Journal of The
Electrochemical Society

Analytical and Fast Numerical Models for PEM Fuel Cell Impedance with Damjanović Kinetics of the Oxygen Reduction Reaction

To cite this article: Andrei Kulikovsky 2025 *J. Electrochem. Soc.* **172** 124508

Journal of The Electrochemical Society, 2025 **172** 124508

Analytical and Fast Numerical Models for PEM Fuel Cell Impedance with Damjanović Kinetics of the Oxygen Reduction Reaction

Andrei Kulikovsky[*,z]

Forschungszentrum Jülich GmbH, Theory and Computation of Energy Materials, (IET–3), Institute of Energy and Climate Research, D–52425 Jülich, Germany

The impedance spectra of many PEM fuel cells exhibit a low-frequency inductive loop. Among possible mechanisms of the loop formation is the slow dynamics of the oxygen reduction reaction (ORR) intermediates on the platinum surface. Because of the time required to change the coverage of species adsorbed on the platinum surface, variations in cell potential do not lead to an immediate response in cell current. This results in inductive-type impedance behavior. In this work, we rederive the previously obtained solutions to the equations describing the Damjanović kinetics of the ORR. We report corrected analytical solutions for the steady-state surface coverages of intermediate species and for the small AC perturbation amplitudes of the coverages. Based on these solutions, a fast analytical model for the ORR impedance is developed. Fitting the ORR impedance model to experimental spectra of a rotating disk electrode is demonstrated. Further, incorporation of the ORR kinetics into analytical and numerical models for PEM fuel cell impedance is performed. The numerical model is fitted to the experimental impedance spectra of a button-size PEM fuel cell. In the limit of zero frequency, the model converges to the DC cell resistivity determined from the polarization curve.
 [DOI: 10.1149/1945-7111/ae26d1]

Manuscript submitted September 25, 2025; revised manuscript received November 18, 2025. Published December 10, 2025.

Nomenclature

~	Marks dimensionless variables
^	Marks dimensionless current density and impedance in Section IIIA
b_1, b_3	Tafel slope of the steps 1 and 3, respectively (V)
C_{dl}	Double layer volumetric capacitance, F cm^{-3}
c_{ox}	Local oxygen molar concentration in the CCL (mol cm^{-3})
c_{ref}	Reference oxygen concentration (mol cm^{-3})
c_p	Proton molar concentration in the CCL, mol cm^{-3}
c_1	Oxygen concentration at the CCL/GDL interface (mol cm^{-3})
D_{ox}	Oxygen diffusion coefficient in the CCL (cm^2 s^{-1})
F	Faraday constant
i_*	ORR volumetric exchange current density (A cm^{-3})
j	Proton current density (A cm^{-2})
j_0	Cell or electrode current density (A cm^{-2})
$\widetilde{K}_i$	Dimensionless forward rate constant of the ith step
$\tilde{k}_1, \tilde{k}_3$	Dimensionless pre–exponential factors in the expressions for the rate constants $\widetilde{K}_1$ and $\widetilde{K}_3$
l_t	Catalyst layer thickness (cm)
Q	Dimensionless function, Eq. 51
R_{ORR}	Total rate of the ORR, (A cm^{-3})
$\tilde{r}_2$	Dimensionless rate constant of the reverese step 2
r_b	Ratio of the Tafel slopes b_1/b_3
t	Time (s)
x	Coordinate through the CCL counted from the membrane (cm)
Z	Impedance (Ω cm^2)

Subscripts

0	Electrolyte/CL interface
1	First reaction step; CCL/GDL interface
2, 3	Second and third reaction steps
ccl	Cathode catalyst layer
dl	Double layer
ox	Oxygen
ref	Reference value
t	Catalyst layer
*	Characteristic value

Superscripts

0	Steady–state
1	Small perturbation

Greek

Γ_s	Number of active Pt sites per electrode unit volume, mol cm^{-3}
γ_s	Number of Pt sites per unit catalyst surface, mol cm$^{-2}_{Pt}$
η	Local overpotential in the CCL (V)
η_0	Total polarization overpotential (V)
θ_a	OH surface coverage
θ_b	O_2H surface coverage
θ_f	Fraction of free sites on Pt surface
μ	Dimensionless constant, Eq. 46
ν_i	Volumetric frequency of the ith reaction step, mol cm^{-3} s^{-1}
ε	Newman's dimensionless reaction penetration depth, Eq. 46
σ_p	CCL proton conductivity (Ω^{-1} cm^{-1})
ω	Angular frequency, s^{-1}

In recent years, polymer electrolyte membrane (PEM) fuel cells appeared on the market of power sources for heavy-duty trains, ships and trucks.[1] The mobile applications require fast methods for cell/stack diagnostics and analysis. The Electrochemical Impedance Spectroscopy (EIS)[2] is, perhaps, the best tool for this task.

An impedance spectrum of a PEM fuel cell contains a lot of valuable information on the processes inside the cell. However, extraction of this information is a difficult task. Over the past two decades, a distribution of relaxation times (DRT) technique of spectra analysis has become widespread. The DRT is a model-free, purely math procedure of impedance spectrum expansion into an infinite sum of parallel RC-circuit impedances.[3–5] This procedure is fast and in some cases it gives the characteristic frequencies and resistivities of the transport and kinetic processes in the cell.

However, the classic DRT is unable to handle the inductive processes in the cell. Nyquist spectra of PEM fuel cells often exhibit a low-frequency inductive loop,[6] which cannot be expanded into *RC*–circuit elements. Recently, novel kernels for the DRT have been

*Electrochemical Society Member.
[z]E-mail: A.Kulikovsky@fz-juelich.de

proposed aiming to include the inductive components into impedance expansion.[7–9] The applicability of new kernels still is a subject of ongoing research.

Physics-based modeling of the cell impedance is free from this limitation. Generally, any transient performance model of the cell can be used to calculate impedance either directly, or after a preliminary analytical work. Direct numerical approach implies application of harmonic AC perturbation of potential or current and solution of model equations in the time domain. The impedance is then calculated from a numerical Fourier transform of the applied perturbation and the cell response.[10] Alternatively, the system of transient performance equations can be linearized and Fourier-transformed analytically to get the system of linear equations for the perturbation amplitudes. Numerical,[11–20] or in some cases, analytical solutions[21–23] to this system give the cell impedance.

The nature of the inductive loop in the impedance spectra has long been a subject of discussions in literature. Antoine, Bultel and Durand[12] and Makharia, Mathias and Baker[24] attributed the inductive behavior to the slow dynamics of ORR intermediates on Pt surface. Roy and Orazem[15] and Roy, Orazem and Tribollet[25] have shown that formation of hydrogen peroxide and Pt dissolution lead to inductive loop. Setzler and Fuller[18] developed a detailed physics–based impedance model that accounted for Pt oxidation and demonstrated the formation of the LF loop due to this process. However, no attempts have been reported yet to fit this model to experimental spectra.

Kulikovsky[26] and Sun et al.[27] have reported the formation of an inductive loop due to the slow relaxation of the CCL water content. The CCL ionic conductivity is proportional to the water content. Due to this coupling, a change in the proton current is delayed with respect to the change in potential, indicating inductive behavior. Analytical[26] and numerical[27] spectra demonstrate the inductive loop. Reshetenko et al.[28] have fitted the model[27] to experimental spectra and proposed a mechanism of the CCL oxygen diffusivity variation with the current density.

Makharia, Mathias and Baker[24] reported a large gap between the measured lowest frequency impedance and the cell DC resistivity determined from the polarization curve. This gap indicates the presence of a process with the characteristic frequency below the lowest frequency achieved in their EIS measurements. Recently, the experiments of Gerling et al.[29] confirmed the presence of the gap and demonstrated that it does not vanish down to the cell current density of about 10 mA cm^{-2}. The authors[29] developed a simplified impedance model of the CCL, which included partial coverage of Pt surface by OH species. A qualitative similarity between the model and experimental spectra has been demonstrated.

In this work, we consider the ORR kinetics mechanism proposed by Damjanović et al.[30,31] We rederive analytical solutions[32] to this problem. Corrected solutions are used to develop a fast analytical model for the ORR impedance. The model is fitted to experimental spectra obtained with a rotating disk electrode (RDE). Further, we incorporate the ORR impedance model into a model for PEM fuel cell impedance. The numerical impedance model is then fitted to spectra measured from a button-size PEM fuel cell. The fitted model well describes the inductive loop and it gives the cell static resistivity, which is close to the DC resistivity determined from the polarization curve.

Model for ORR Kinetics

Reaction scheme and kinetic equations.—The ORR reaction scheme considered below consists of three steps:

$$O_2(g) + H^+ + e^- + \text{Site} \xrightarrow{k_1} (O_2H)_{ads} \qquad [1]$$

$$(O_2H)_{ads} + H_2O + \text{Site} + \text{Site} \underset{r_2}{\overset{k_2}{\rightleftarrows}} 3(OH)_{ads} \qquad [2]$$

$$(OH)_{ads} + H^+ + e^- \xrightarrow{k_3} H_2O + \text{Site} \qquad [3]$$

In the first step, gaseous oxygen is transformed into adsorbed $(O_2H)_{ads}$ via a single-electron transfer Eq. 1. In the second chemical step $(O_2H)_{ads}$ and water molecule produce three adsorbed OH species. Finally, the OH species are converted into a water in a single-electron transfer step Eq. 3.

Damjanović et al. proposed the first and final steps in the ORR chain. The same steps have been considered in a modeling study of Jinnouchi et al.[33] The intermediate chemical step 2 is the simplest mechanism for converting adsorbed $(O_2H)_{ads}$ into $(OH)_{ads}$. Other conversion mechanisms are discussed in.[33,34]

Our ultimate goal is to incorporate ORR impedance into the PEM fuel cell impedance model. Therefore, it is convenient to work with the volumetric frequencies of the steps 1–3 per unit of porous electrode volume. Let the rates of steps 1–3 be ν_1, ν_2 and ν_3, (mol cm^{-3} s^{-1}). Assuming that the steps 1 and 3 are shifted toward reduction, we write the rates ν_i in the form

$$\nu_1 = k_1 c_{ox} c_p \theta_f \exp\left(\frac{\eta}{b_1}\right) \qquad [4]$$

$$\nu_2 = k_2 c_w \theta_b \theta_f^2 - r_2 \theta_a^3 \qquad [5]$$

$$\nu_3 = k_3 c_p \theta_a \exp\left(\frac{\eta}{b_3}\right) \qquad [6]$$

where

$$\theta_f = 1 - \theta_a - \theta_b \qquad [7]$$

is the fraction of free Pt sites, c_{ox}, c_w and c_p are the molar concentrations of oxygen, liquid water and protons, respectively, θ_a and θ_b are the surface coverages of the adsorbed OH and O_2H species, respectively, k_1, k_2, r_2, k_3 are the rate constants. For simplicity, Eqs. 4–6 are written assuming the Langmuir adsorption isotherm. This is a first step toward a more accurate model that would include the effects of lateral interaction and non-ideal adsorption.

Kinetic equations for the surface coverages are

$$\Gamma_s \frac{\partial \theta_a}{\partial t} = 3\nu_2 - \nu_3 \qquad [8]$$

$$\Gamma_s \frac{\partial \theta_b}{\partial t} = \nu_1 - \nu_2 \qquad [9]$$

where

$$\Gamma_s = \gamma_s S_{ECSA} L_{Pt}/l_t, \quad \text{mol cm}^{-3} \qquad [10]$$

is the number of active Pt sites per unit electrode volume. Here, $\gamma_s = 2.18 \times 10^{-9}$ mol cm_{Pt}^{-2} is the number of sites per unit catalyst surface,[35] S_{ECSA} is the electrochemical surface area of the dispersed Pt (cm_{Pt}^2 mg_{Pt}^{-1}), L_{Pt} is the Pt loading per unit of electrode surface (mg_{Pt} cm^{-2}), and l_t is the electrode thickness.

The ORR rate R_{ORR} is given by

$$R_{ORR} = F(\nu_1 + \nu_3) \ \text{A cm}^{-3}. \qquad [11]$$

Below, the following dimensionless variables will be used

$$\tilde{t} = \frac{t}{t_{dl}}, \tilde{\eta} = \frac{\eta}{b_1}, \hat{j} = \frac{j}{i_* l_t}, \tilde{c}_{ox} = \frac{c_{ox}}{c_{ref}}, \tilde{\omega} = \omega t_{dl},$$
$$\widehat{Z} = \frac{Z i_* l_t}{b_1} \quad [12]$$

where

$$t_{dl} = \frac{C_{dl} b_1}{i_*} \quad [13]$$

is the characteristic time of the double layer charging, η is the positive by convention overpotential, j is the local proton current density, i_* is the volumetric ORR exchange current density (A cm^{-3}), c_{ref} is the reference oxygen concentration, l_t is the CCL thickness, b_1 is the Tafel slope of the first step, C_{dl} is the volumetric DL capacitance (F cm^{-3}).

With Eq. 12, the Eqs. 8 and 9 transform to the dimensionless form:

$$\frac{\partial \theta_a}{\partial \tilde{t}} = 3\widetilde{K}_2 \theta_b \theta_f^2 - 3\widetilde{R}_2 \theta_a^3 - \widetilde{K}_3 \theta_a \quad [14]$$

$$\frac{\partial \theta_b}{\partial \tilde{t}} = \widetilde{K}_1 \theta_f - \widetilde{K}_2 \theta_b \theta_f^2 + \widetilde{R}_2 \theta_a^3 \quad [15]$$

where θ_f is given by Eq. 7 and the dimensionless rate constants $\widetilde{K}_1$, $\widetilde{K}_2$, $\widetilde{R}_2$, $\widetilde{K}_3$ are given by

$$\widetilde{K}_1 = \Gamma_s^{-1} t_{dl} k_1 c_{ox} c_p \exp\left(\frac{\eta}{b_1}\right) = \tilde{k}_1 \tilde{c}_{ox} \exp\left(\frac{\eta}{b_1}\right),$$
$$\widetilde{K}_2 = \Gamma_s^{-1} t_{dl} k_2 c_w = \tilde{k}_2,$$
$$\widetilde{R}_2 = \Gamma_s^{-1} t_{dl} r_2 = \tilde{r}_2,$$
$$\widetilde{K}_3 = \Gamma_s^{-1} t_{dl} k_3 c_p \exp\left(\frac{\eta}{b_3}\right) = \tilde{k}_3 \exp\left(\frac{\eta}{b_3}\right) \quad [16]$$

with

$$\tilde{k}_1 = \Gamma_s^{-1} t_{dl} k_1 c_{ref} c_p, \quad \tilde{k}_3 = \Gamma_s^{-1} t_{dl} k_3 c_p, \quad [17]$$

Steady–state solutions.—Consider first a steady–state solution to the system of Eqs. 14, 15. Removing the time derivatives, we come to

$$3\widetilde{K}_2 \theta_b \theta_f^2 - 3\widetilde{R}_2 \theta_a^3 - \widetilde{K}_3 \theta_a = 0 \quad [18]$$

$$\widetilde{K}_1 \theta_f - \widetilde{K}_2 \theta_b \theta_f^2 + \widetilde{R}_2 \theta_a^3 = 0 \quad [19]$$

Multiplying Eq. 19 by 3 and summing with Eq. 18, we get

$$3\widetilde{K}_1(1 - \theta_a - \theta_b) - \widetilde{K}_3 \theta_a = 0, \quad [20]$$

which gives a linear relation between θ_b and θ_a. Using this relation, it is easy to show that the system 18, 19 has two pairs of exact solutions that differ in sign at the square root:

$$\theta_a^{0+} = \frac{p_{13}}{2u}(1 + \sqrt{1 - 4p_{12}u})$$
$$\theta_b^{0+} = 1 - \left(1 + \frac{1}{p_{13}}\right)\theta_a^{0+} \quad [21]$$

and

$$\theta_a^{0-} = \frac{p_{13}}{2u}(1 - \sqrt{1 - 4p_{12}u})$$
$$\theta_b^{0-} = 1 - \left(1 + \frac{1}{p_{13}}\right)\theta_a^{0-} \quad [22]$$

where the superscript 0 indicates the steady–state solutions, and we have introduced notations

$$u = 1 + p_{13}\left(1 + \frac{p_{13}^2}{p_{22}}\right) \quad [23]$$

$$p_{12} \equiv \frac{\widetilde{K}_1}{\widetilde{K}_2}, \quad p_{13} \equiv \frac{3\widetilde{K}_1}{\widetilde{K}_3}, \quad p_{22} \equiv \frac{\widetilde{K}_2}{\widetilde{R}_2} \quad [24]$$

We can express p_{12} and p_{13} through the overpotential

$$p_{12} = \frac{\tilde{k}_1 \tilde{c}_{ox}}{\tilde{k}_2} \exp\left(\frac{\eta}{b_1}\right)$$
$$p_{13} = \frac{3\tilde{k}_1 \tilde{c}_{ox}}{\tilde{k}_3} \exp\left(\frac{\eta}{b_1} - \frac{\eta}{b_3}\right) \quad [25]$$

At steady–state, $\nu_3 = 3\ \nu_2$, $\nu_2 = \nu_1$ and Eq. 11 reduces to the static ORR rate

$$R_{ORR}^0 = 4F\nu_1 \quad [26]$$

where the superscript 0 indicates the steady–state value. With Eq. 4, we can write Eq. 26 in a conventional form

$$R_{ORR}^0 = i_*\left(\frac{c_{ox}}{c_{ref}}\right)\theta_f^{0+} \exp\left(\frac{\eta^0}{b_1}\right) \quad [27]$$

where $\theta_f^{0+} = 1 - \theta_a^{0+} - \theta_b^{0+}$ is the steady-state fraction of free Pt sites, and

$$i_* = 4Fk_1 c_{ref} c_p \quad [28]$$

is the volumetric exchange current density (A cm^{-3}). In the following, the superscript $^+$ will be omitted, $\theta^0 \equiv \theta^{0+}$. Note that θ_f^0 in Eq. 27 is a function of the overpotential $\tilde{\eta}^0$.

Limits of validity of the steady-state solutions.—The steady-state solutions 21 and 22 exist provided that the expression $1 - 4p_{12}u$ under the square root is nonnegative:

$$4p_{12}\left(1 + p_{13}\left(1 + \frac{p_{13}^2}{p_{22}}\right)\right) \leqslant 1 \quad [29]$$

If $b_1 < b_3$, this condition determines the limiting overpotential. Indeed, Eqs. 25, 24 show that p_{12} increases with the overpotential η, while p_{22} is independent of η. Furthermore, for $b_1 < b_3$, the parameter p_{13} also grows with η. Thus, at some $\eta = \eta_{\text{lim}}$ the left side of Eq. 29 exceeds unity, meaning that for all $\eta > \eta_{\text{lim}}$, the steady–state solution to the system 14, 15 does not exist. Physically, for $\eta > \eta_{\text{lim}}$, the rate of the reaction 1 exceeds the rate of the chemical step 2, which leads to full blocking of the catalyst surface by O_2H species. Analysis of the solutions type for this case is out of the scope of the present work.

In the opposite case of $b_1 > b_3$, the parameter p_{13} decreases with the overpotential and the model may work at the highest

overpotentials provided that the parameter $\tilde{k}_2$ is sufficiently large. When $b_1 > b_3$, the rate of step 3 increases with overpotential faster than the rate of step 1. If the rate of the chemical step 2 is high enough to prevent the Pt surface from being blocked by O_2H species, the model works well for all realistic overpotentials.

In general, the two pairs of solutions, 21 and 22, indicate that the system may exhibit bistability, that is, two steady-state solutions may coexist. However, an analysis quite analogous to[32] shows that, over a broad range of kinetic parameters, the solution Eq. 22 is unstable. Numerical tests show that Eq. 22 describe a metastable state. The system remains in this state for a finite amount of time. Eventually, however, it transforms into the stable state described by Eq. 21. For further calculations we will use Eq. 21.

Solution for perturbation amplitudes.—The amplitude of applied AC signal is small; thus, we may write

$$\tilde{\eta} = \tilde{\eta}^0 + \tilde{\eta}^1, \quad \theta_a = \theta_a^0 + \theta_a^1, \quad \theta_b = \theta_b^0 + \theta_b^1 \qquad [30]$$

where, as before, the superscripts 0 and 1 mark the steady–state variables and small perturbations, respectively. Substituting Eq. 30 into Eqs. 14, 15, neglecting the terms with the perturbation products, and subtracting the respective steady–state equations, we get a linear system for the perturbations:

$$\begin{aligned} \frac{\partial \theta_a^1}{\partial \tilde{t}} &= a_{11}\theta_a^1 + a_{12}\theta_b^1 - f_1\tilde{\eta}^1 \\ \frac{\partial \theta_b^1}{\partial \tilde{t}} &= a_{21}\theta_a^1 + a_{22}\theta_b^1 - f_2\tilde{\eta}^1 \end{aligned} \qquad [31]$$

where the coefficients a_{11}, a_{12}, a_{21}, a_{22}, f_1, and f_2 are given in Appendix A.

The applied perturbation is harmonic; hence we may write

$$\begin{aligned} \tilde{\eta}^1(\tilde{t}) &= \tilde{\eta}^1(\tilde{\omega})\exp(\mathrm{i}\tilde{\omega}\tilde{t}), \\ \theta_a^1(\tilde{t}) &= \theta_a^1(\tilde{\omega})\exp(\mathrm{i}\tilde{\omega}\tilde{t}), \\ \theta_b^1(\tilde{t}) &= \theta_b^1(\tilde{\omega})\exp(\mathrm{i}\tilde{\omega}\tilde{t}) \end{aligned} \qquad [32]$$

Substituting Eq. 32 into Eq. 31, we get a system of linear algebraic equations for the perturbation amplitudes in the ω–space:

$$\begin{aligned} (a_{11} - \mathrm{i}\tilde{\omega})\theta_a^1 + a_{12}\theta_b^1 &= f_1\tilde{\eta}^1 \\ a_{21}\theta_a^1 + (a_{22} - \mathrm{i}\tilde{\omega})\theta_b^1 &= f_2\tilde{\eta}^1 \end{aligned} \qquad [33]$$

Solution to the system 33 reads

$$\begin{aligned} \theta_a^1 &= \frac{(a_{12}f_2 - a_{22}f_1 + \mathrm{i}\tilde{\omega}f_1)\tilde{\eta}^1}{\tilde{\omega}^2 + a_{12}a_{21} - a_{11}a_{22} + (a_{11} + a_{22})\mathrm{i}\tilde{\omega}} \\ \theta_b^1 &= \frac{(a_{21}f_1 - a_{11}f_2 + \mathrm{i}\tilde{\omega}f_2)\tilde{\eta}^1}{\tilde{\omega}^2 + a_{12}a_{21} - a_{11}a_{22} + (a_{11} + a_{22})\mathrm{i}\tilde{\omega}} \end{aligned} \qquad [34]$$

ORR rate perturbation.—To calculate the ORR rate perturbation, we must use the general Eq. 11, which is valid under transient conditions. Substituting Eqs. 4, 6 into 11 and taking into account 28, we get

$$\begin{aligned} R_{ORR} &= F\left(k_1 c_{ox} c_p \theta_f \exp\left(\frac{\eta}{b_1}\right) + k_3 c_p \theta_a \exp\left(\frac{\eta}{b_3}\right)\right) \\ &= \frac{i_*}{4}\left(\left(\frac{c_{ox}}{c_{ref}}\right)\theta_f \exp\left(\frac{\eta}{b_1}\right) + a_* \theta_a \exp\left(\frac{\eta}{b_3}\right)\right) \end{aligned} \qquad [35]$$

where i_* is given by Eq. 28 and

$$a_* = \frac{k_3}{k_1 c_{ref}} = \frac{\tilde{k}_3}{\tilde{k}_1} \qquad [36]$$

With the dimensionless variables Eqs. 12, 35 takes the form

$$\widetilde{R}_{ORR} = \frac{1}{4}\left(\tilde{c}_{ox}\theta_f \exp(\tilde{\eta}) + a_*\theta_a \exp(r_b\tilde{\eta})\right) \qquad [37]$$

where $\widetilde{R}_{ORR} = R_{ORR}/i_*$ and $r_b = b_1/b_3$.

Linearization anf Fourier transform of Eq. 37 give equation for the ORR perturbation amplitude:

$$\begin{aligned} \widetilde{R}_{ORR}^1 = \frac{1}{4}\theta_f^0 \mathrm{e}^{\tilde{\eta}^0}\tilde{c}_{ox}^1 + \frac{1}{4}\Bigg\{\tilde{c}_{ox}^0 \mathrm{e}^{\tilde{\eta}^0}\left(\frac{\theta_f^1}{\tilde{\eta}^1} + \theta_f^0\right) \\ + a_* \exp(r_b\tilde{\eta}^0)\left(\frac{\theta_a^1}{\tilde{\eta}^1} + \theta_a^0 r_b\right)\Bigg\}\tilde{\eta}^1 \end{aligned} \qquad [38]$$

Eq. 34 show that $\theta_a^1 \sim \tilde{\eta}^1$ and $\theta_b^1 \sim \tilde{\eta}^1$ and hence the expression in figure brackets in Eq. 38 is independent of $\tilde{\eta}^1$.

Impedance Models

Impedance of a rotating disk electrode.—For a thin electrode operating in the kinetic regime (high potential), the oxygen and proton transport losses inside the electrode can be neglected. The proton charge conservation equation is

$$l_t C_{dl}\frac{\partial \eta}{\partial t} - j_0 = -l_t R_{ORR} \qquad [39]$$

where j_0 is the current density. With the dimensionless variables Eqs. 12, 39 takes the form

$$\frac{\partial \tilde{\eta}}{\partial \tilde{t}} - \hat{j}_0 = -\widetilde{R}_{ORR} \qquad [40]$$

Linearization and Fourier-transform of Eq. 40 leads to

$$\mathrm{i}\tilde{\omega}\tilde{\eta}^1 - \hat{j}^1 = -\widetilde{R}_{ORR}^1 \qquad [41]$$

Dividing both sides of Eq. 41 by $\tilde{\eta}^1$, we get the equation for electrode impedance $\widehat{Z}$

$$\mathrm{i}\tilde{\omega} - \frac{1}{\widehat{Z}} = -\frac{\widetilde{R}_{ORR}^1}{\tilde{\eta}^1}. \qquad [42]$$

As discussed above, in this Section we assume that the static oxygen concentration $\tilde{c}_{ox}^0$ is independent of the coordinate through the electrode $\tilde{x}$ and equal to the oxygen concentration at the electrode/electrolyte interface $\tilde{c}_1^0$. Further, since the oxygen transport is fast, the term with $\tilde{c}_{ox}^1$ in Eq. 38 can be neglected. From Eqs. 42 and 38 we finally get

$$\begin{aligned} \widehat{Z} &= 1 \Bigg/ \left(\mathrm{i}\tilde{\omega} + \frac{\tilde{c}_1^0 \mathrm{e}^{\tilde{\eta}^0}}{4}\left(\frac{\theta_f^1}{\tilde{\eta}^1} + \theta_f^0\right) + \frac{a_*}{4}\exp(r_b\tilde{\eta}^0)\left(\frac{\theta_a^1}{\tilde{\eta}^1} + \theta_a^0 r_b\right)\right) \\ \widehat{Z} &= \frac{Zi_* l_t}{b_1}. \end{aligned} \qquad [43]$$

Here the frequency-dependent parameters θ_a^1, θ_b^1, $\theta_f^1 = -\theta_a^1 - \theta_b^1$ are given by Eq. 34, and the static parameters θ_a^0, θ_b^0, $\theta_f^0 = 1 - \theta_a^0 - \theta_b^0$ are given by Eq. 21.

Equation 43 is an analytical model for the impedance of the electrode operating in the kinetic regime. Fitting of Eq. 43 to the experimental spectra of Choudhury et al.[36] is discussed in Section IVA.

Impedance of the cathode catalyst layer in a PEM fuel cell.— Generally, in a PEM fuel cell the oxygen and proton transport through the CCL depth cannot be ignored. The equations for the overpotential $\tilde{\eta}^1$ and oxygen concentration $\tilde{c}_{ox}^1$ perturbation amplitudes in the CCL are[23]

$$\mathrm{i}\tilde{\omega}\tilde{\eta}^1 - \varepsilon^2\frac{\partial^2\tilde{\eta}^1}{\partial\tilde{x}^2} = -\widetilde{R}_{ORR}^1 \qquad [44]$$

$$\mathrm{i}\tilde{\omega}\mu^2\tilde{c}_{ox}^1 - \varepsilon^2\widetilde{D}_{ox}\frac{\partial^2\tilde{c}_{ox}^1}{\partial\tilde{x}^2} = -\widetilde{R}_{ORR}^1 \qquad [45]$$

where $\tilde{x}$ is the coordinate through the CCL with the origin at the membrane surface and $\tilde{x} = 1$ at the CCL/GDL interface, and

$$\varepsilon = \sqrt{\frac{\sigma_p b_1}{i_* l_t^2}}, \quad \mu = \sqrt{\frac{4Fc_{ref}}{C_{dl}b_1}}. \qquad [46]$$

Note that here, the current density is scaled as

$$\tilde{j} = \frac{j}{j_*}, \quad j_* = \frac{\sigma_p b_1}{l_t} \qquad [47]$$

which differs from the scaling in Eq. 12.

Equation 38 for $\widetilde{R}_{ORR}^1$ is ready for using in Eqs. 44, 45. With Eq. 38, Eqs. 44, 45 can be written in the form suitable for the fast matrix solver[37]

$$\frac{\partial^2\tilde{\eta}^1}{\partial\tilde{x}^2} = p\tilde{c}_{ox}^1 + q\tilde{\eta}^1, \quad \tilde{\eta}^1(1) = \tilde{\eta}_1^1, \quad \left.\frac{\partial\tilde{\eta}^1}{\partial\tilde{x}}\right|_{\tilde{x}=1} = 0 \qquad [48]$$

$$\frac{\partial^2\tilde{c}_{ox}^1}{\partial\tilde{x}^2} = r\tilde{c}_{ox}^1 + s\tilde{\eta}^1, \quad \left.\frac{\partial\tilde{c}_{ox}^1}{\partial\tilde{x}}\right|_{\tilde{x}=0} = 0, \quad \tilde{c}_{ox}^1(1) = \tilde{c}_1^1 \qquad [49]$$

where $\tilde{\eta}_1^1$ is the applied small perturbation, the coefficient functions p, q, r, s are

$$p = \frac{\theta_f^0 \mathrm{e}^{\tilde{\eta}^0}}{\varepsilon^2}, \quad q = \frac{Q + \mathrm{i}\tilde{\omega}}{\varepsilon^2}$$
$$r = \frac{\theta_f^0 \mathrm{e}^{\tilde{\eta}^0}/4 + \mathrm{i}\tilde{\omega}\mu^2}{\varepsilon^2\widetilde{D}_{ox}}, \quad s = \frac{Q}{\varepsilon^2\widetilde{D}_{ox}} \qquad [50]$$

and Q is the coefficient at $\tilde{\eta}^1$ in Eq. 38:

$$Q = \frac{\tilde{c}_{ox}^0 \mathrm{e}^{\tilde{\eta}^0}}{4}\left(\frac{\theta_f^1}{\tilde{\eta}^1} + \theta_f^0\right) + \frac{a_*}{4}\exp(r_b\tilde{\eta}^0)\left(\frac{\theta_a^1}{\tilde{\eta}^1} + \theta_a^0 r_b\right) \qquad [51]$$

The CCL impedance is given by

$$\widetilde{Z}_{ccl} = -\left.\frac{\tilde{\eta}^1}{\partial\tilde{\eta}^1/\partial\tilde{x}}\right|_{\tilde{x}=0}, \quad \widetilde{Z} = \frac{Z\sigma_p}{l_t} \qquad [52]$$

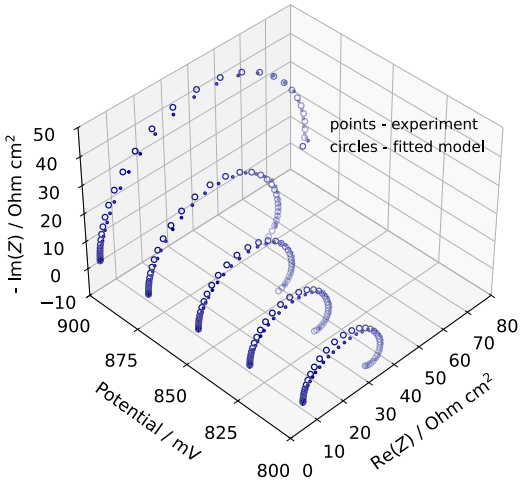

Figure 1. The fitted model Eq. 43 (open circles) and the experimental (solid points) Nyquist spectra of the rotating disk ORR electrode.[36]

Note that here the scaling of $\widetilde{Z}$ differs from the scaling of $\widehat{Z}$ in Section IIIB.

Fully analytical model for PEMFC impedance.—If the cell current is small, the variation of the static ORR overpotential $\tilde{\eta}^0$ and oxygen concentration $\tilde{c}_{ox}^0$ through the electrode depth can be ignored. In this case, the parameters p, q, r, s, Eq. 50, are independent of the coordinate $\tilde{x}$. These parameters can be used instead of Eq. 15 in Ref. 23 resulting in a very fast, fully analytical model for the PEMFC cathode side impedance. This model takes into account the proton transport in the CCL, the oxygen transport in the channel, gas-diffusion and catalyst layers, and the ORR kinetics discussed above.

Below, we will consider a more general case of medium to large cell current densities, where the variation of $\tilde{\eta}^0$ and $\tilde{c}_{ox}^0$ in the CCL cannot be neglected. In this case, p, q, r, and s depend on the coordinate $\tilde{x}$. Numerical solutions to Eqs. 48, 49 can be obtained using the fast matrix solver.[37]

Results and Discussion

Fitting RDE impedance spectra.—Choudhury et al.[36] reported impedance measurements of a rotating disk ORR electrode in $HClO_4$ electrolyte. The electrode was prepared using unsupported Pt black dissolved in isopropyl alcohol. This mixture was drop-cast onto a polished glassy carbon disk electrode and dried. With the electrode surface area of 0.196 cm^2, the total Pt loading of 0.125 $mg_{Pt}cm^{-2}$ (Ref. 36) and the Pt black density of $0.65 \cdot 10^3$ $mg_{Pt}cm^{-3}$, the estimated catalyst layer thickness is $l_t = 1.92$ μm. The RDE was placed in an oxygen-saturated 0.1 M solution of $HClO_4$ and impedance measurements were performed for the frequencies down to 20 mHz. Other experimental details can be found in Ref. 36. In the previous work from this group, the RDE-based spectra have been analyzed using an equivalent circuit method.[38]

It is difficult to estimate the oxygen diffusivity of unsupported Pt-based CL. The spectra[36] measured in the potential range of 900 to 800 mV suggest that the contribution of oxygen transport inside the electrode to the impedance is small. However, the spectra measured at the potentials below 800 mV exhibit a quite significant oxygen transport contribution, which increases as the potential decreases.[36]

The Nyquist spectra of the model Eq. 43 fitted to the experimental spectra are shown in Fig. 1. Fitting has been performed using a custom Python code (see the next section). Figure 2 shows a detailed view of the Nyquist and Bode plots of the spectra for an electrode

Table I. Parameters for the fitted impedance curves in Fig. 1. The last column shows the estimated fitting quality χ^2/N, where N is the number of points in the spectrum. The last two rows show the mean values and their standard deviation. To obtain the Tafel slopes b_1 and b_3 in mV/dec, the values in Table should be multiplied by 2.3.

Potential mV	$\tilde{k}_1$	$\widetilde{K}_2$	$\widetilde{R}_2$	$\tilde{k}_3$	b_1 mV/exp	b_3 mV/exp	χ^2/N Ω^2 cm^4
800	1.32e-3	3.24e4	2.81e3	18.5	28.4	87.6	2.95
825	9.52e-4	4.00e4	8.09e3	12.4	26.8	79.3	2.93
850	6.57e-4	3.03e4	9.52e3	11.6	25.3	81.1	2.81
875	4.58e-4	3.29e4	1.12e4	15.0	23.7	98.9	2.41
900	5.84e-4	3.88e3	2.25e3	27.7	22.4	120	1.11
mean:	7.9e-4	2.8e4	6.8e3	17.0	25.3	93.4	
std. dev.:	3.5e-4	1.4e4	4.0e3	6.5	2.4	17	

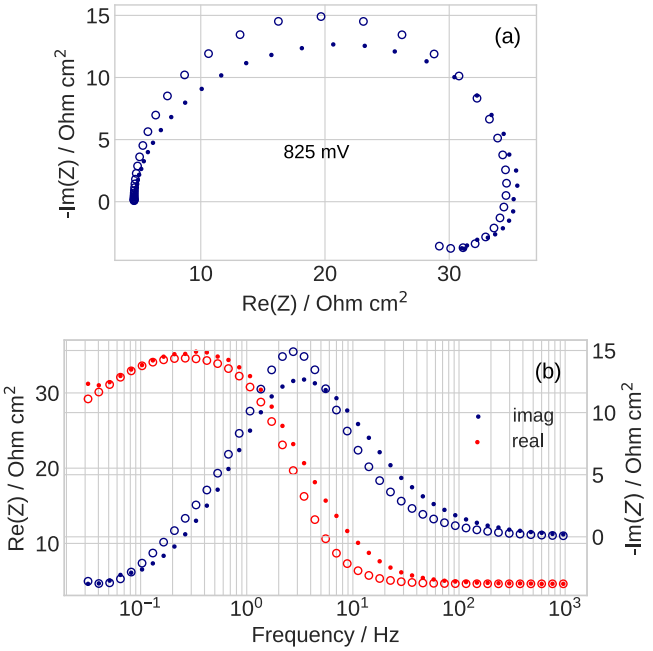

Figure 2. (a) The fitted model Eq. 43 (open circles) and the experimental (solid points) Nyquist spectra of the RDE for the electrode potential of 825 mV.[36] (b) The Bode plots of the real and imaginary part of the spectra in (a).

potential of 825 mV. As can be seen, the low-frequency loop has a characteristic frequency of about 40 mHz (minimum of -Im(Z) in Fig. 2b). This corresponds to a time constant of $\tau_{ads} \simeq 1/(6.28 \cdot 0.04) \simeq 4$ s. Reducing the electrode potential to 800 mV decreases the time constant to about 1 s, indicating that the ORR runs faster at higher currents.

The quality of spectra fitting in Figs. 1, 2 is not perfect. One possible reason for this is the nonuniform thickness of the catalyst layer over the electrode surface, as unsupported Pt black tends to agglomerate. The dimensionless kinetic coefficients obtained from fitted spectra are collected in Table I. The mean values of all the coefficients are determined with a reasonably good accuracy. The lower accuracy of $\widetilde{R}_2$ can be explained by a small contribution of the reverse step 2 to the impedance.

Fitting PEM fuel cell impedance spectra.—Recently, Butori et al.[39] published the impedance spectra of a button-size PEM fuel cell with an active area of 0.95 cm^2. The commercial MEA used in the experiments was based on the reinforced PFSA membrane. The MEA had a membrane with the thickness of $\simeq$9 μm and a $\simeq$8.3–μm thick Pt/C cathode catalyst layer. The operating regime of the cell during the EIS measurements is indicated in Table II. Spectra were measured at a cell current density of 100 mA cm^{-2} with an air feed at cathode

Table II. The cell operating and fitted parameters.

Abs. cathode pressure/bar	1.0	2.0
Anode/cathode feed	H_2/air	H_2/air
Current density, A cm^{-2}	0.1	0.1
Cathode relative humidity RH	0.7	0.8
Cell temperature, K	353	353
Cathode flow stoichiometry	52	52
CCL thickness, μm	8.3	8.3
Fitted parameters:		
CCL proton conductivity, mS cm^{-1}	4.2	3.9
DL capacitance, F cm^{-3}	13.7	14.8
CCL oxygen diffusivity, 10^{-4} cm^2 s^{-1}	0.697	0.449

pressures of 1 and 2 bar. The air flow stoichiometry was approximately 50. More experimental details can be found in Ref. 39.

Before fitting, the high-frequency inductive cable impedance $i\omega L_{cab} S_{cell}$ has been subtracted from the cell impedance. Here, $L_{cab} = 120$ nH is the cable inductance and S_{cell} is the cell active area. Since the air flow stoichiometry is large and the current is small, the contribution of oxygen transport in the channel and gas diffusion layer to the impedance has been neglected. The cell impedance was calculated as

$$Z_{cell} = \frac{l_t \widetilde{Z}_{ccl}}{\sigma_p} + R_{HFR} \qquad [53]$$

where $\widetilde{Z}_{ccl}$ is given by Eq. 52 and the cell ohmic resistivity R_{HFR} is included in the list of fitting parameters.

Fitting has been performed using a custom Python code. Nonlinear BVPs for the steady-state oxygen concentration $\tilde{c}^0$ and overpotential $\tilde{\eta}^0$ shapes through the CCL depth (Appendix B) were solved using the *solve_bvp* routine from the SciPy library. Linear BVPs for the perturbation amplitudes, Eqs. 48, 49, were solved using the fast matrix solver.[37] This technique allows to estimate the numerical performance of the model for the general case of variable with $\tilde{x}$ static oxygen concentration $\tilde{c}^0$ and overpotential $\tilde{\eta}^0$.

Programming of the model equations for the steady-state surface coverages and their perturbation amplitudes takes about 20 lines of Python code. If the expression $(1 - 4p_{12}u)$ under the square root in Eq. 21 becomes negative, it is recommended to set $\theta_a^0 = 0$, $\theta_b^0 = 1$, and $\theta_f^0 = 0$. This "tells" the fitting procedure that the Pt surface is fully blocked by O_2H species.

The full list of experimental conditions is presented in Table III. The experimental and fitted spectra measured at the cathode pressure of 1 and 2 bar are shown in Figs. 3 and 4, respectively. As can be seen the quality of fitting is very good through the whole frequency range. The kinetic coefficients for the fitted spectra are collected in

Table III. Parameters for the fitted impedance curves in Figs. 3 (1 bar) and 4 (2 bar). To obtain the Tafel slopes b_1 and b_3 in mV/dec, the values in Table should be multiplied by 2.3.

Pressure bar	$\tilde{k}_1$	$\widetilde{K}_2$	$\widetilde{R}_2$	$\tilde{k}_3$	b_1 mV/exp	b_3 mV/exp
1	9.11e-4	5.44e5	890	9.11	27.9	76.0
2	8.34e-4	3.07e5	343	18.3	22.8	72.3

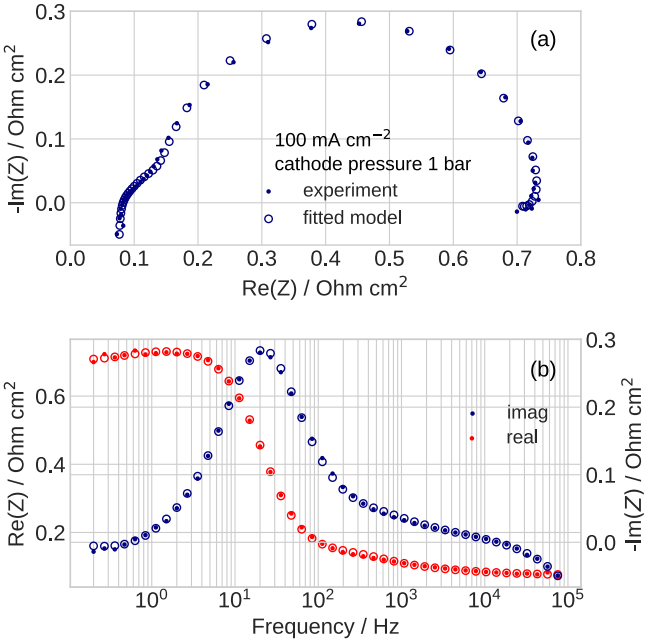

Figure 3. (a) The experimental (solid points) and fitted model Eq. 52 (open circles) Nyquist spectra of the button PEM fuel cell.[39] The cell temperature is 80 °C, the cathode pressure is 1 bar and RH = 70%. (b) The respective Bode plots of the real and imaginary parts of the impedance.

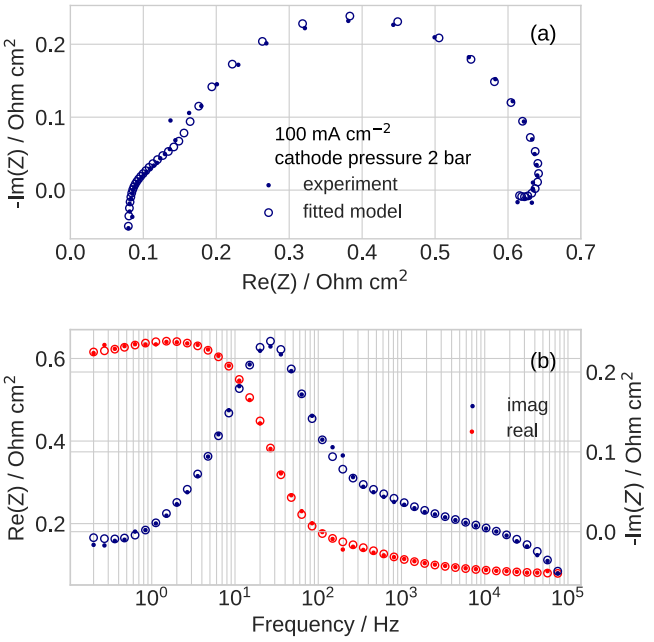

Figure 4. The experimental (solid points) and fitted model Eq. 52 (open circles) Nyquist spectra of the button PEM fuel cell.[39] The cell temperature is 80 °C, the cathode pressure is 2 bar and RH = 80%. (b) The respective Bode plots of the real and imaginary parts of impedance in (a).

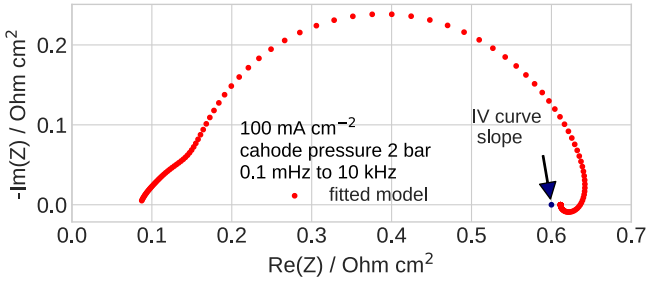

Figure 5. The fitted model Nyquist spectrum in Fig. 4a calculated in the frequency range from 0.1 mHz to 10 kHz. The arrow indicates the DC resistance calculated from the slope of polarization curve (see text).

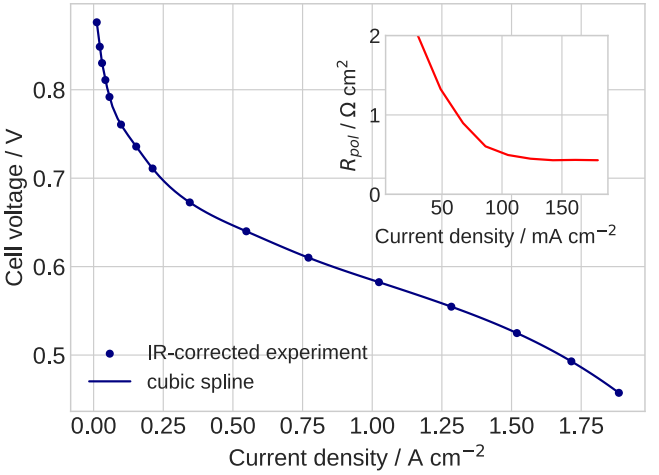

Figure 6. The experimental (points) and interpolated (solid line) IR-corrected polarization curves of the cell. The experimental points were digitized from the blue curve in Fig. 3c of Ref. 39 . The cell temperature 80 °C, the cathode pressure 2 bar and RH = 80%. The inset: the cell polarization resistivity R_{pol} calculated as the first derivative of the cubic spline interpolating the IV curve. At 100 mA cm^{-2}, the sum $R_{pol} + R_{HFR}$ of 600 mOhm cm^2 is indicated with the arrow in Fig. 5.

Table III. The minimum of $-\mathrm{Im}Z$ in Fig. 4b shows that the characteristic frequency of the inductive process is around 50 mHz. This value agrees well with the one obtained from fitting the RDE spectrum (Fig. 2b) indicating that the LF loop in the cell spectra is most probably due to ORR kinetics.

Figure 5 shows the model Nyquist spectrum from Fig. 4 calculated for the frequencies down to 0.1 mHz. The spectrum displays the model DC resistivity of the cell, which is achieved as the frequency approaches zero. The slope of the IR-corrected experimental polarization curve at the current density of 100 mA cm^{-2} is 512 mOhm cm^2 (inset in Fig. 6). The slope was calculated as the first derivative of the cubic spline interpolating the experimental IR-corrected polarization curve (Fig. 6). With the cell ohmic resistivity of 88 mOhm cm^2 (Fig. 5), the experimental DC resistivity of the cell is $88 + 512 = 600$ mOhm cm^2. The impedance model gives the DC resistivity of 611 mOhm cm^2, which agrees well with the experiment (Fig. 5).

Finally, we note that the model does not take into account the effects of Pt oxidation and peroxide formation, which could affect the cell impedance. Incorporation of these effects will be addressed in future work.

Conclusions

We rederive analytical solutions reported in[32] to the equations for Damjanović kinetics of the oxygen reduction reaction. Using the corrected solutions, an analytical model for the ORR impedance is developed. Fitting of the model to experimental spectra from the rotating disk electrode is demonstrated. Further, the ORR impedance

model is incorporated into the analytical and fast numerical models for PEM fuel cell impedance. The numerical model is fitted to the spectra with an inductive loop measured from the button-size PEM fuel cell. A high quality of fitting the spectra is shown. In the DC limit, the fitted model converges to the true DC cell resistivity, which is determined from the polarization curve. Fitting the PEMFC impedance model to an experimental spectrum takes just several seconds on a standard 4.4 GHz notebook.

Acknowledgments

The author is grateful to Prof. M. Neergat and Dr. Choudhury (Indian Inst. of Technology, Bombay) for the numerical data of the spectra measured with RDE. Many thanks to Dr. M. Butori (KTH Royal Inst. of Technology, Stockholm) for the experimental spectra of a small PEMFC. Useful discussions with Dr. Olga Baturina (Naval Research Labs, Washington DC) are greatly appreciated.

Appendix A. Dimensionless Coefficients in Eqs. 31 and 33

The coefficients in the system of Eq. 31 are

$$
\begin{aligned}
a_{11} &= -6\widetilde{K}_2^0\theta_f^0\theta_b^0 - 9\widetilde{R}_2^0(\theta_a^0)^2 - \widetilde{K}_3^0\\
a_{12} &= 3\widetilde{K}_2^0\theta_f^0\left(\theta_f^0 - 2\theta_b^0\right)\\
a_{21} &= -\widetilde{K}_1^0 + 2\widetilde{K}_2^0\theta_f^0\theta_b^0 + 3\widetilde{R}_2^0(\theta_a^0)^2\\
a_{22} &= -\widetilde{K}_1^0 - \widetilde{K}_2^0\theta_f^0\left(\theta_f^0 - 2\theta_b^0\right)\\
f_1 &= \widetilde{K}_3^0 r_b\theta_a^0\\
f_2 &= -\widetilde{K}_1^0\theta_f^0
\end{aligned}
\qquad [A\cdot1]
$$

and

$$
\begin{aligned}
\theta_f^0 &= 1 - \theta_a^0 - \theta_b^0,\\
\theta_f^1 &= -\theta_a^1 - \theta_b^1.
\end{aligned}
\qquad [A\cdot2]
$$

Appendix B. Steady State Problem

The dimensionless problem for the static overpotential $\tilde{\eta}^0$ and oxygen concentration $\tilde{c}^0$ in the CCL is

$$
\begin{aligned}
&\varepsilon^2\frac{\partial^2\tilde{\eta}^0}{\partial\tilde{x}^2} = \tilde{c}^0\theta_f^0\exp\tilde{\eta}^0,\\
&\left.\frac{\partial\tilde{\eta}^0}{\partial\tilde{x}}\right|_{\tilde{x}=0} = -\tilde{j}_0,\ \left.\frac{\partial\tilde{\eta}^0}{\partial\tilde{x}}\right|_{\tilde{x}=1} = 0
\end{aligned}
\qquad [B\cdot1]
$$

$$
\widetilde{D}_{ox}\frac{\partial\tilde{c}^0}{\partial\tilde{x}} = \tilde{j}_0 - \tilde{j}^0,\quad \tilde{c}^0(1) = \tilde{c}_1^0
\qquad [B\cdot2]
$$

where $\tilde{j}_0$ is the DC cell current density and $\tilde{c}_1^0$ is the oxygen concentration at the CCL/GDL interface. Equation B.1 is the proton charge conservation equation. Equation B.2 expresses the local balance of the oxygen flux and proton current density. With the Ohm's law $\tilde{j}^0 = -\partial\tilde{\eta}^0/\partial\tilde{x}$, Eqs. B.1, B.2 is a closed-form problem.

ORCID

Andrei Kulikovsky https://orcid.org/0000-0003-1319-576X

References

1. Ö. F. Günaydin, S. Topçu, and A. Aksoy, "Hydrogen fuel cell vehicles: Overview and current status of hydrogen mobility." *Int. J. Hydrogen Energy*, **142**, 918 (2025).
2. A. Lasia, *Electrochemical Impedance Spectroscopy and its Applications* (Springer, New York) (2014).
3. R. M. Fuoss and J. G. Kirkwood, "Electrical properties of solids:. VIII. Dipole moments in polyvinyl chloride-diphenyl systems." *J. Am. Chem. Soc.*, **63**, 385 (1941).
4. H. Schichlein, A. C. Müller, M. Voigts, A. Krügel, and E. Ivers-Tiffée, "Deconvolution of electrochemical impedance spectra for the identification of electrode reaction mechanisms in solid oxide fuel cells." *J. Appl. Electrochem.*, **32**, 875 (2002).
5. E. Ivers-Tiffée and A. Weber, "Evaluation of electrochemical impedance spectra by the distribution of relaxation times." *J. Ceramic Soc. Japan*, **125**, 193 (2017).
6. I. Pivac and F. Barbir, "Inductive phenomena at low frequencies in impedance spectra of proton exchange membrane fuel cells - A review." *J. Power Sources*, **326**, 112 (2016).
7. M. A. Danzer, "Generalized distribution of relaxation times analysis for the characterization of impedance spectra." *Batteries*, **5**, 1 (2019).
8. C. Plank, T. G. Bergmann, N. Schlüter, and M. A. Danzer, "Distribution of relaxation times analysis for impedance spectra containing resistive-inductive characteristics: Part I. Deconvolution methods." *J. Electrochem. Soc.*, **172**, 060514 (2025).
9. T. Reshetenko and A. Kulikovsky, "A comparison of PEM fuel cell parameters resulting from the distribution of relaxation times, distribution of transport times, and physics-based modeling." *Electrochim. Acta*, **543**, 147529 (2025).
10. Y. Shi, N. Cai, C. Li, C. Bao, E. Croiset, J. Qian, Q. Hu, and S. Wang, "Simulation of electrochemical impedance spectra of solid oxide fuel cells using transient physical models." *J. Electrochem. Soc.*, **155**, B270 (2008).
11. T. E. Springer, T. A. Zawodzinski, M. S. Wilson, and S. Gottesfeld, "Characterization of polymer electrolyte fuel cells using AC impedance spectroscopy." *J. Electrochem. Soc.*, **143**, 587 (1996).
12. O. Antoine, Y. Bultel, and R. Durand, "Oxygen reduction reaction kinetics and mechanism on platinum nanoparticles inside Nafion." *J. Electroanal. Chem.*, **499**, 85 (2001).
13. Y. Bultel, L. Genies, O. Antoine, P. Ozil, and R. Durand, "Modeling impedance diagrams of active layers in gas diffusion electrodes: Diffusion, ohmic drop effects and multistep reactions." *J. Electroanal. Chem.*, **527**, 143 (2002).
14. F. Jaouen and G. Lindbergh, "Transient techniques for investigating mass-transport limitations in gas diffusion electrodes." *I modelind the PEFC cathode. J. Electrochem. Soc.*, **150**, A1699 (2003).
15. S. K. Roy and M. E. Orazem, "Deterministic impedance models for interpretation of low frequency inductive loops in PEM fuel cells." *ECS Trans*, **3**, 1031 (2006).
16. D. Gerteisen, A. Hakenjos, and J. O. Schumacher, "AC impedance modelling study on porous electrodes of proton exchange membrane fuel cells using an agglomerate model." *J. Power Sources*, **173**, 346 (2007).
17. G. Maranzana, J. Mainka, O. Lottin, J. Dillet, A. Lamibrac, A. Thomas, and S. Didierjean, "A proton exchange membrane fuel cell impedance model taking into account convection along the air channel: On the bias between the low frequency limit of the impedance and the slope of the polarization curve." *Electrochim. Acta*, **83**, 13 (2012).
18. B. P. Setzler and T. F. Fuller, "A physics-based impedance model of proton exchange membrane fuel cells exhibiting low-frequency inductive loops." *J. Electrochem. Soc.*, **162**, F519 (2015).
19. F. Ciucci, "Modeling electrochemical impedance spectroscopy." *Current Opinion in Electrochem*, **13**, 132 (2018).
20. A. Kulikovsky and O. Shamardina, "A model for PEM fuel cell impedance: Oxygen flow in the channel triggers spatial and frequency oscillations of the local impedance." *J. Electrochem. Soc.*, **162**, F1068 (2015).
21. A. Baricci and A. Casalegno, "A simple analytical approach to simulate the electrochemical impedance response of flooded agglomerates in polymer fuel cells." *Electrochim. Acta*, **157**, 324 (2015).
22. D. Vivona, A. Casalegno, and A. Baricci, "Validation of a pseudo 2D analytical model for high temperature PEM fuel cell impedance valid at typical operative conditions." *Electrochim. Acta*, **310**, 122 (2019).
23. A. Kulikovsky, "Analytical impedance of PEM fuel cell cathode including oxygen transport in the channel, gas diffusion and catalyst layers." *J. Electrochem. Soc.*, **169**, 034527 (2022).
24. R. Makharia, M. F. Mathias, and D. R. Baker, "Measurement of catalyst layer electrolyte resistance in PEFCs using electrochemical impedance spectroscopy." *J. Electrochem. Soc.*, **152**, A970 (2005).
25. S. K. Roy, M. E. Orazem, and B. Tribollet, "Interpretation of low-frequency inductive loops in PEM fuel cells." *J. Electrochem. Soc.*, **154**, B1378 (2007).
26. A. Kulikovsky, "Effect of proton conductivity transients on PEM fuel cell impedance: Formation of a low-frequency inductive loop." *Electrochem. Comm.*, **140**, 107340 (2022).
27. Y. Sun, T. Kadyk, A. Kulikovsky, and M. Eikerling, "The effect of liquid saturation transients on PEM fuel cell impedance: Inductive loop and instability of catalyst layer operation." *J. Electrochem. Soc.*, **171**, 074506 (2024).
28. T. Reshetenko, Y. Sun, T. Kadyk, M. Eikerling, and A. Kulikovsky, "An impedance spectroscopy study to unravel the effect of water on proton and oxygen transport in PEM fuel cells." *Electrochim. Acta*, **507**, 145172 (2024).
29. C. Gerling, M. Hanauer, U. Berner, and K. A. Friedrich, "Experimental and numerical investigation of the low-frequency inductive features in differential pemfcs: Ionomer humidification and platinum oxide effects." *J. Electrochem. Soc.*, **170**, 014504 (2023).
30. A. Damjanovic and V. Brusic, "Electrode kinetics of oxygen reduction on oxide-free platinum electrodes." *Electrochimica Acta*, **12**, 615 (1967).
31. H. Wroblowa, M. L. B. Rao, A. Damjanovic, and J. O. M. Bockris, "Adsorption and kinetics at platinum electrodes in the presence of oxygen at zero net current." *J. Electroanal. Chem.*, **15**, 139 (1967).

32. A. A. Kulikovsky, "Analysis of Damjanovi'c kinetics of the oxygen reduction reaction: Stability, polarization curve and impedance spectra." *J. Electroanal. Chem.*, **738**, 130 (2015).
33. R. Jinnouchi, K. Kodama, T. Hatanaka, and Y. Morimoto, "First principles based mean field model for oxygen reduction reaction." *Phys. Chem. Chem. Phys.*, **13**, 21070 (2011).
34. A. Kriston, B. B. Berkes, P. L. Simion, G. Inzelt, K. Dobos, and A. Nemes, "Unusual surface mass changes in the course of the oxygen reduction reaction on platinum and their explanation by using a kinetic model." *J. Solid State Electrochem.*, **16**, 1723 (2012).
35. P. I. Giotakos and S. G. Neophytides, "Physical modeling of the electrochemical impedance spectra for the O_2 reduction reaction in HTPEM fuel cells' cathodic electrochemical interface." *Electrochim. Acta*, **292**, 285 (2018).
36. D. Choudhury, R. Das, R. Maurya, G. Gupta, and M. Neergat, "Low-frequency inductive features in the electrochemical impedance spectra of mass-transport limited redox reactions." *Phys. Chem. Chem. Phys.*, **25**, 10966 (2023).
37. A. Kulikovsky, "A fast matrix solver for linear boundary-value problem in the PEM fuel cell impedance model." *Electrochem. Soc. Adv.*, **3**, 034503 (2024).
38. R. K. Singh, R. Devivaraprasad, T. Kar, A. Chakraborty, and M. Neergat, "Electrochemical impedance spectroscopy of oxygen reduction reaction (orr) in a rotating disk electrode configuration: Effect of ionomer content and carbon-support." *J. Electrochem. Soc.*, **162**, F489 (2015).
39. M. Butori, B. Eriksson, N. Nikolić, C. Lagergren, G. Lindbergh, and R. W. Lindström, "The effect of oxygen partial pressure and humidification in proton exchange membrane fuel cells at intermediate temperature (80–120 °C)." *J. Power Sources*, **563**, 232803 (2023).